Contents lists available at ScienceDirect

Composites Part A

A fatigue test based on inclined loading block concept to benchmark delamination growth considering loading history and $\mathcal{R}$-curve effect

I. Leciñana [a,b], J. Renart [b,c,*], L. Carreras [b], A. Turon [b], J. Zurbitu [a], B.H.A.H. Tijs [d,e]

[a] IKERLAN Technology Research Centre, Basque Research and Technology Alliance (BRTA), Gipuzkoa, Spain
[b] AMADE, Polytechnic School, University of Girona, C/Universitat de Girona 4, 17003 Girona, Spain
[c] Serra Húnter Fellow, Generalitat de Catalunya, Spain
[d] Fokker/GKN Aerospace, Anthony Fokkerweg 4, 3351 NL, Papendrecht, The Netherlands
[e] Faculty of Aerospace Engineering, Delft University of Technology, Kluyverweg 1, 2629 HS Delft, The Netherlands

ARTICLE INFO

ABSTRACT

The main objective of this paper is to present a delamination benchmark test concept for composite materials that develop non-self-similar delamination in characterization specimens. The non-self-similar delamination is induced by rotating the loading blocks. The simplicity of the test allows for analyzing the loading mode history by concatenating different loading conditions, such as static and fatigue loading, under multiple loading modes. The methodology introduced in this paper can be particularized for any given composite material set and any sequence of loading conditions. To demonstrate the capabilities of the benchmark test, a case study is presented using AS4D/PEKK-FC thermoplastic composite material, which exhibits strong R-curve behavior. A sequence of opening and shear failure modes was applied under static and fatigue loading, providing an experimental data set that is ready to be used as a part of the validation of numerical predictive delamination models. The delamination process was monitored by X-ray radiography, and the final fracture surfaces were analyzed with scanning electron microscopy (SEM), giving a physical insight into the contribution of the fracture mechanisms to the delamination process.

1. Introduction

The transport industry is increasingly moving towards more optimized and lightweight structures [1]. Cost-efficient and sustainable designs must meet structural integrity and reliability [2,3]. To this end, experimental testing is the basis in which state-of-the-art design tools are developed, providing characterization and validation data.

Characterization methodologies for delamination onset and propagation of composite material under different loading conditions have been widely studied in literature over the past decades [4–12]. Characterization tests are usually performed in geometrically simple specimens, and data reduction schemes are used trying to synthesize the whole test into some experimental constants that are assumed to be material properties. However, some simplifications are sometimes made which are not representative of the in-service loading conditions. For example, characterization tests can be approximated to a 2D loading scenario, and they do not consider the transient effects of alternating different loading conditions such as (a) static and fatigue loading, (b) amplitudes in fatigue loading (load interaction effects), and (c) alternating different loading modes. Moreover, in fracture characterization

tests, self-similar damage evolution is generally assumed, collapsing the whole fracture process zone and using linear elastic fracture mechanics approaches [13–15].

Characterization tests are used to obtain material properties that can be implemented into phenomenological models to predict the behavior of structures. To ensure that the designs are both reliable and optimized, the predictive capabilities of the models and the significance of the experimental characterizations must be validated. Some works in literature verify their models by simulating the characterization tests from which the material properties were obtained [16–19]. However, this practice cannot be considered as a validation of the model because it may result in not evaluating the aforementioned important effects that structures withstand under in-service loading conditions. The shortcomings of only verifying the predictive tools against characterization tests get accentuated when using composite materials that exhibit resistance curve ($\mathcal{R}$-curve) influence, since transient effects are more significant. This is the case of new generation thermoplastic resins [20,21], which exhibit strong $\mathcal{R}$-curve influence due to fiber bridging and/or plastic strain.

A significant validation test must allow to measure and have a full understanding of the relationship between the applied boundary conditions and the consequent damage evolution/delamination process. The test must also achieve a compromise between simplicity of testing and faithful representation of the failure mechanisms involved during in-service application. However, there are not many examples in the literature where these features are met. Regarding validation tests that consider the 3D effects of a structure, a benchmark test for mode I fatigue delamination based on the concept of the reinforced DCB specimen (R-DCB) was first developed for an epoxy/carbon fiber material system [22]. A non-self-similar delamination with a curved and shape-shifting crack front due to the 3D geometry was achieved under static and fatigue loading. The delamination front was monitored by means of X-ray radiography, although other non-destructive inspection techniques such as acoustic emissions (AE) [23] could be used to capture the 3D delamination process. The same concept was replicated for a glass fiber R-DCB which exhibited large-scale fiber bridging [24]. In this case, an automated digital image-based method was used to track the delamination front. In [25], unnotched and open-hole composite specimens were statically tested under sub-critical traction and compression loading. Damage evolution was monitored to obtain model validation data: damage location, amount, stiffness loss, and strength loss. It can be concluded that there is a rather limited number of examples of validation tests in which a complete understanding of the correlation between applied boundary conditions and damage evolution in composite structures under a realistic 3D state of loading is achieved. Moreover, in the existing validation tests, the testing configuration is limited by the specimen geometry, and therefore, a different specimen is required to have a new test configuration.

Concerning validation tests that take into account the contribution of fatigue amplitude, Jensen et al. investigated the influence of fatigue delamination of step changes in block amplitude loading [26]. An analysis of the transient delamination growth under variable amplitude loading in G-control [27] was performed by the same authors. The effect of variable amplitude block loading on intralaminar crack initiation and propagation in multi-directional laminates was analyzed in [28,29]. Recently [30] correlated the measured strain energy release rate in a fatigue cycle with acoustic emission measurements concluding that the applied fatigue loading amplitude influences the activation of different damage mechanism thresholds, having an impact in delamination resistance. It must be mentioned that all these investigations were performed under mode I loading resulting in a 2D load case scenario, while there are no 3D case studies.

Regarding the influence of loading mode history, while brittle matrix cracking and fiber bridging are dominant under mode I loading, plastic deformation and the creation of hackles ahead of the crack tip due to shear stresses dominate the shear mode delamination [31]. In mixed-mode loading, failure mechanisms of both pure loading modes are present to some extent as a function of the mixed-mode ratio. Even if characterization tests and data reduction methods that analyze the coupled effect of mode I and shear mode loading are available in literature [32–35], there is a limited amount of investigation regarding how a material zone damaged by a certain loading mode behaves under a different loading mode. A round-robin test campaign was presented in [36], investigating different pre-cracking modes applied to mode II or mixed mode tests. It was found that fracture toughness values from pre-cracks were lower than those from inserts and that there is little difference between mode I and mode II pre-cracks. Considering the limited amount of data, and since the material damages in a certain way to resist a given loading mode, it is worth investigating the response of the material when different loading modes are applied consecutively at a partially developed delamination process zone.

This feature is of great interest when working with composite materials that exhibit strong $\mathcal{R}$-curve effects. $\mathcal{R}$-curves of materials are triggered by the activation of different failure mechanisms, and are characterized from standardized fracture tests. Recent works have developed models to consider the $\mathcal{R}$-curve effect as a function of the loading mode angle (mode I - mode II) [37–39] based on Benzeggagh and Kenane (B-K) criterion [40]. However, this approach does not consider the effect of concatenating a given loading mode after the other, nor the effect of mode III.

In this work, a novel delamination test concept is introduced based on mode I and mode II characterization tests, where the boundary conditions are modified by rotating the loading blocks of the test rig with respect to the longitudinal axis of the specimen. Developing this concept, a benchmark test where the combined transient effects of (a) 3D loading scenario, (b) alternating static and multiple amplitude fatigue loading, and (c) alternating different loading modes during non-self-similar delamination processes (loading mode history) are analyzed. Moreover, the benchmark test does not just give information from the crack tip location, but it also gives qualitative information on the fracture process zone evolution using X-ray radiography data and *post mortem* SEM images. To demonstrate the capabilities of the benchmark test, a case study is performed on a AS4D/PEKK-FC thermoplastic composite, where a sequence of mode I and shear mode loading (combined effects of mode II and mode III) under static and fatigue conditions is applied.

This paper is structured as follows: in Section 2, the test concept to achieve the non-self-similar 3D delamination process in characterization specimens is explained. In Section 3, the methodology used to perform the validation case study is developed, detailing the material system, the boundary conditions, the loading sequence, and the test monitoring procedure. In Section 4, the results of the validation case study are presented. In Section 5, the influence and mechanics of the delamination process zone during the 3D non-self-similar delamination under complex loading conditions are discussed. Finally, the conclusions are presented in Section 6.

2. Non-self-similar delamination in characterization specimens

In this section, a new delamination test concept for composite materials is introduced. The boundary conditions yield a non-self-similar delamination process in simple characterization specimens that cannot be simplified as a 2D loading case. It is understood as a non-self-similar delamination process when the delamination growth driving direction [41] of a local point within the delamination process zone is different with respect to (a) the growth driving direction of the leading delamination tip and (b) the growth driving direction of other points within the process zone. For example, in Fig. 1b, the delamination growth driving direction of the local point D is different from the growth driving directions of the leading delamination tip (point C) and another point in the process zone (point E).

Given a DCB specimen starting from the insert, if a standardized mode I or mode II test is performed [13,15], the delamination will grow parallel to the longitudinal axis of the specimen. This is achieved thanks to applying the boundary conditions perpendicular to the longitudinal axis of the specimen, imposing a homogeneous distribution of strain energy release rate (SERR) along the delamination front.

However, if the loading fixtures are set so that they both form an α angle with respect to the perpendicular of the longitudinal axis of the specimen, a SERR gradient is imposed along the delamination front (Fig. 1a). Therefore, the growth driving direction of the delamination leading tip will evolve differently from the specimen's longitudinal direction as the delamination occurs. As the delamination process zone evolves, the different local points within the process zone will have a different growth driving direction with respect to the leading tip growth driving direction as well as with respect to other local points' growth driving directions (Fig. 1b).

Besides, if the material being tested has significant $\mathcal{R}$-curve effects, as a fracture process zone is created under a non-self-similar delamination process, the development of the $\mathcal{R}$-curve is dissimilar at different delamination process segments. The $\mathcal{R}$-curve evolution state
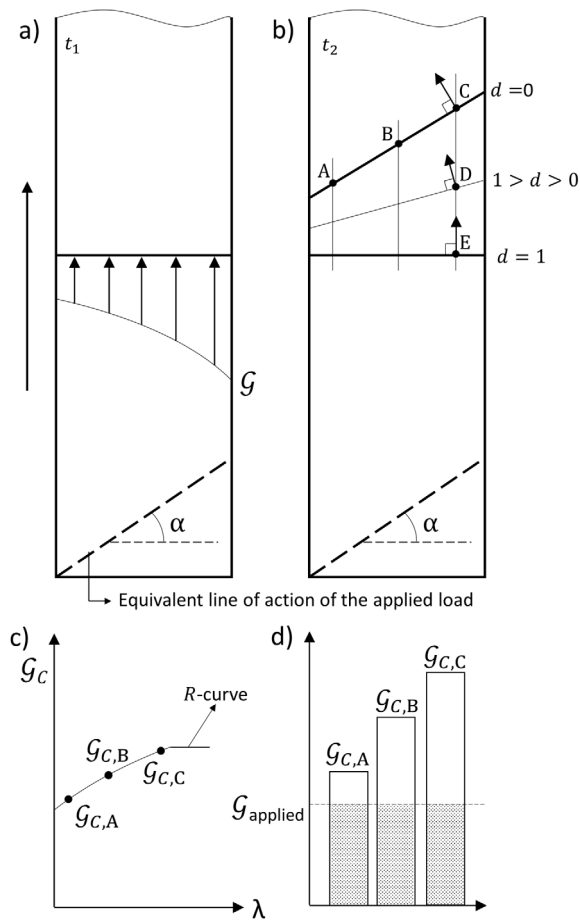
Fig. 1. (a) Strain energy release rate gradient achieved by rotating the loading fixture an α angle, where the arrow outside the specimen indicates the delamination propagation direction, which is defined by the longitudinal axis of the specimen, (b) Representation of a non-self-similar delamination process that cannot be simplified as a 2D loading case because at each delamination state, each material point has a delamination direction which is defined locally. The local delamination direction might be different from the delamination propagation direction defined by the longitudinal axis of the specimen, (c) Dissimilar evolution of the $\mathcal{R}$-curve along the process zone, (d) Dissimilar SERR severities as a function of $\mathcal{R}$-curve development states.

Table 1
AS4D/PEKK-FC thermoplastic composite elastic properties at room temperature [20]:

Property	Description	Value	Unit
E_{1t}	Young's modulus, fiber tensile direction	138 300	MPa
E_{2t}	Young's modulus, matrix tensile direction	10 400	MPa
$G_{12} = G_{13}$	Shear modulus	5190	MPa
ν_{12}	Poisson ratio, 1–2 direction	0.316	–
ν_{23}	Poisson ratio, 2–3 direction	0.487	–

3. Benchmark test

In this section, a delamination benchmark test for composite materials is presented. The inclined loading block test concept is used to apply different loading modes under different loading conditions (static and fatigue).

The proposed methodology is exemplified with the AS4D/PEKK-FC thermoplastic composite material. All necessary experimental data for validating predictive models under a multi-mode static and fatigue loading sequence in a material with $\mathcal{R}$-curve effects is described in the next subsections.

3.1. Material properties

The material used in this work is the Solvay (formerly Cytec) APC (PEKK-FC) thermoplastic polymer prepreg that is a fast-crystallizing thermoplastic matrix of poly ether-ketone-ketone commonly referred to as PEKK-FC, reinforced with a continuous unidirectional AS4D fiber with a nominal ply thickness of 0.138 mm [43]. The elastic properties of the laminate are summarized in Table 1. The interlaminar fracture properties and the standardized characterization procedures are listed in Table 2.

3.2. Specimen design

Standard characterization specimens were used in the benchmark test [13,15]. An AS4D/ PEKK-FC flat panel that consists of 30 unidirectional plies was manufactured through autoclave consolidation, using a curing cycle of a heating ramp of 5 °C/min, an iso-thermal stage at 377 °C of at least 45 min, and a cool-down speed in the order of 5 °C/min. The specimens were not preconditioned before testing. From that flat panel, a batch of specimens was machined. The specimens were designed to be 25 mm wide and 225 mm long. The thickness of the specimens was about 4.2 mm. Due to the high melting temperature of thermoplastic composites, a 12.5 mu thick UPILEX foil (60 mm long) was used as an insert to start the crack.

3.3. Measuring the delamination process evolution

Radiography was performed using an X-ray source with a maximum power of 20 W, a focal spot of 5 μm, and a 2400 × 2400 pixel detector manufactured by HAMAMATSU and assembled by NOVADEP Scientific Instruments. X-ray images were captured using the settings 35 kV, 120 μA, and analogue integration of 5 images, with each image exposed for 3 s. To improve X-ray contrast, a solution containing 520 g of zinc iodide, 86.5 ml of distilled water, 86.5 ml of alcohol, and 26 ml of Kodak Photo-Flo 200 was utilized [22]. During X-ray imaging, the specimen arms were opened using a wedge and the solution was applied between the specimen arms using a pipette, the specimen was located vertically to ensure the contrast solution reached the front of the delamination gravitationally. The opening imposed with the wedge was 1 mm, having a negligible impact on creep and/or visco-elastic behavior of the material during the X-ray measurements. The whole process of acquiring each radiography image was less than 2 min. Also, the contrast solution has not been reported to impact the delamination

of segments A, B, and C in Fig. 1b are represented in Fig. 1c. Therefore, a fracture toughness gradient will be formed along the width of the specimen due to the dissimilar $\mathcal{R}$-curve evolution.

As a consequence of the dissimilar development of the $\mathcal{R}$-curve along the width of the process zone, under sub-critical fatigue loading conditions, the applied SERR severity ($\mathcal{G}_{\text{applied}}/\mathcal{G}_{C,n}$) is different as a function of the fracture toughness gradient (Fig. 1d), resulting in different fatigue delamination growth rates locally.

The concept of rotating the loading fixture an α angle with respect to the perpendicular of the longitudinal axis of the specimen can be concatenated as many times as desired, changing the value of the angle within the $-180° < \alpha < 180°$ range. This can by easily done just by moving the loading fixture, resulting in an ever-evolving non-self-similar delamination process. Furthermore, static and fatigue loading conditions can be concatenated, and the test can also accommodate variable amplitude and/or simultaneous variable frequency fatigue loading, such as standard flight load spectra.

In order to locate the non-perpendicular delamination front, conventional visual examination of the lateral surfaces is insufficient. More sophisticated approaches are required, such as direct monitoring of the top face of the specimen, as proposed in the study conducted by Bak et al. [42], or utilization of alternative methodologies like X-ray imaging as suggested by Carreras et al. [22].

Table 2
AS4D/PEKK-FC thermoplastic composite fracture properties at room temperature [20,21]:

| Property	Description	Procedure	Value	Unit
$G_{Ic,i}$	Mode I fracture toughness, initiation	ASTMD 5528 [13,20]	0.7	N/mm
$G_{Ic,p}$	Mode I fracture toughness, propagation	ASTMD 5528 [13,20]	1.12	N/mm
$G_{IIc,i}$	Mode II fracture toughness, initiation	ISO 15114 [15,20]	1.45	N/mm
$G_{IIc,p}$	Mode II fracture toughness, propagation	ISO 15114 [15,20]	2.35	N/mm
C_I	Mode I Paris' law coefficient	Multi-fatigue test rig [21]	93.2	mm/cycle
p_I	Mode I Paris' law exponent	Multi-fatigue test rig [21]	8.87	–
C_{II}	Mode II Paris' law coefficient	Multi-fatigue test rig [44]	3.82E−2	mm/cycle
p_{II}	Mode II Paris' law exponent	Multi-fatigue test rig [44]	2.87	–
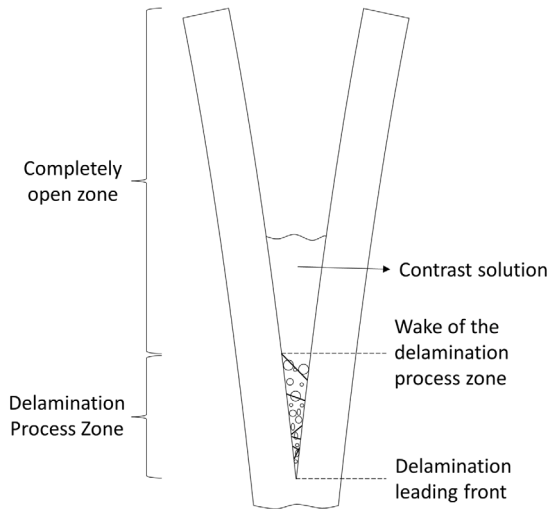
Fig. 2. Sketch of the X-ray inspection with the contrast solution and the damage process zone.

resistance of composite materials [22]. This process was repeated for each measurement.

Transmission X-ray imaging was used to capture images of the specimen, whereby the specimen was positioned between the X-ray transmitter and detector, with the beam crossing the specimen perpendicular to the plane of delamination. Prior to the test, a reference X-ray image of the specimen was taken. The delamination process was assessed at programmed intervals by subtracting the reference image from the current X-ray image. The difference in intensity between both images was only significant at the delaminated region, thanks to the dye solution.

Since the specimen arms were opened with a wedge during X-ray imaging, the attenuation of the X-ray signal due to liquid accumulation decreased as approaching to the delamination leading front, see Fig. 2. This decrease is continuous, and it is the result of the combination of the attenuation constant of the contrast solution, the opening of the arms, and the distance to the leading delamination front. If energy dissipation mechanisms such as micro-cracks, plastic strain, or fiber bridging remain active, they lead to a damage process zone with an accumulation of voids where the liquid can penetrate. There is no longer an empty space to fill in with the liquid but a porous region with different material or void density and, therefore, having different X-ray permeability. This fact allows for detecting deviations in the attenuation signal function.

An automated procedure was developed aiming at detecting both the delamination leading front and the wake of the damage process zone (FPZ). The procedure consisted of discretizing the specimen width in 125 segments and running an image processing algorithm for each segment. The grey-scale value of each pixel was read by the algorithm, creating a contrast signal in each segment, where the pixel length was 4.55 E-2 mm (Fig. 3a). The acquired contrast signal was first smoothed with a low pass filter and then approximated to a moving

linear regression of 99 pixels. Each of the moving linear regression data points comprises the information of the last 0.455 mm of the contrast signal. The data points that met two threshold criteria were set to be the leading delamination front and the wake of the damage process zone: (a) the calculated slope of the moving linear regression deviated from the initial trend and (b) the R^2 of the regression was less than 0.7 for the case of the leading delamination front and less than 0.85 for the case of the wake of the damage process zone (Fig. 3b). The threshold criteria to determine the delamination leading front was set and verified to match the noticeable change in slope of the crossing linear regressions defined in [22]. There was a higher dispersion determining the wake of the process zone, and therefore, setting a threshold was less straightforward. The wake threshold criteria were fit to consistently capture the deviation from the linear regression in several X-ray images that were used as a reference. Since the same threshold was used to determine the wake of the damage zone in all the X-ray images, it is a useful measure to qualitatively analyze the evolution of the damage process zone.

In Fig. 3d, the detected leading delamination tip (black dot) and the wake of the damage process zone (gray cross) points for the 125 segments of an X-ray inspection interval are plotted. The wake of the process zone and the delamination leading tip points delimit the damage process zone. The higher dispersion in the location of the wake of the process zone is understood as inherent to the characteristics of the different damage mechanisms that constitute it.

3.4. Test boundary condition sequence

The following loading sequence was applied to the specimen:

1. The benchmark test started from the insert at an initial crack length a_0 of 41 mm. A mode I pre-crack of 15 mm was performed following the ASTM D5528 standard [13], with the loading block set perpendicular to the longitudinal direction of the specimen. The objective was to create a leading delamination front perpendicular to the longitudinal direction of the specimen with a developed static damage process zone in the wake.
2. Shear mode loading was applied with the ELS test rig specified in the ISO 15114:201 [15] standard, but setting the loading block inclined $+\alpha$ in a counter-clockwise direction with respect to the longitudinal direction of the delamination plane (Fig. 4). The specimen length l from the most distant point of the loading block to the clamping fixture was set to 90 mm, and the distance to the pre-crack, a_0, of 56 mm, ensuring stable delamination and enough distance for the FPZ to fully develop [45]. Shear mode loading was stopped at least 20 mm away from the clamping fixture to avoid any influence of the clamping on the test results.
3. A mode I load was applied using the setup described in ASTM D5528 standard [13] to the existing shear mode leading delamination front. The loading block angle was inverted from $+\alpha$ to $-\alpha$ by pure rotation of the loading blocks with respect to the middle point of the specimen width (clockwise direction) (Fig. 5).

Each time the angle of the load block changes, the load block must be released from the specimen and bonded at the new angle. To simplify this process, the authors suggest using fast-curing adhesives to bond the load blocks to the specimen.
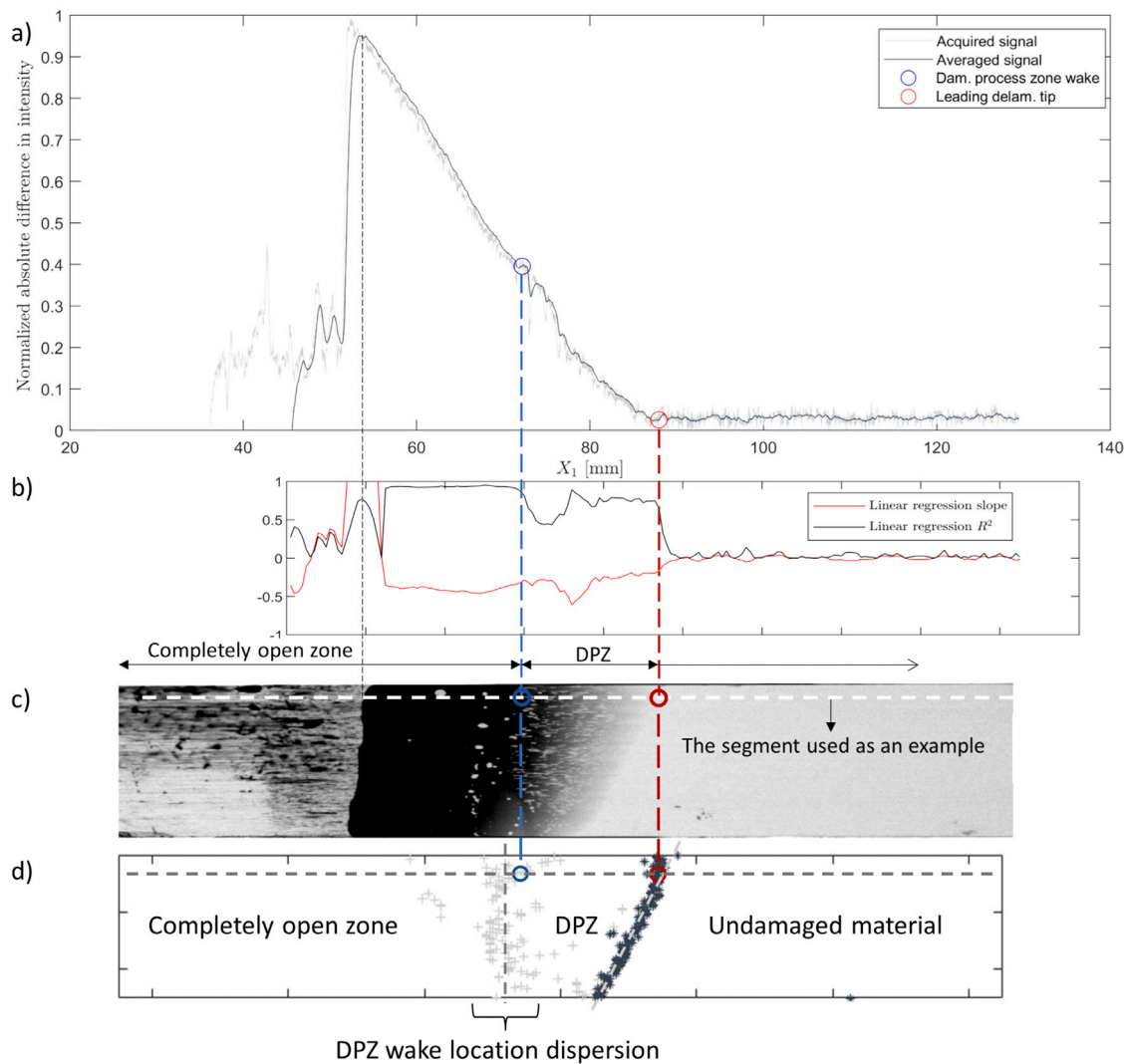
Fig. 3. Automated procedure to detect the leading delamination front and the wake of the damage process zone in X-ray radiography images, based on a moving linear regression of 99 pixels (0.455 mm). (a) acquired contrast signal of a width segment of the specimen extracted from the X-ray gray-scale values, (b) evolution of the moving linear regression slope and R^2 used as threshold criteria to detect the delamination leading tip and the wake of the process zone, (c) gray-scale plot of an X-ray image, and (d) plot of the detected delamination leading tip and the wake of the process zone points for all the segments in an X-ray image.

3.5. Static loading sequence

Following the boundary condition sequence, a fully static test was performed. One specimen was tested under this condition. The static test was performed in laboratory conditions at 23 ± 2 °C and at a RH of $50 \pm 5\%$. The static loading sequence is summarized in Table 3. The exact location of the loading block in each step is defined by the distances set in section 3.4 and the loading angle defined in Table 3. The maximum displacement defined in Table 3 refers to the displacement at the end of each static step, applied at the loading pin (dashed line in Fig. 4). The step name nomenclature gives information regarding the loading is static (S) and is followed by the boundary condition sequence number. In the first step, S.1, a DCB pre-crack was performed at a constant displacement rate of 5 mm/min. The crack front after the pre-crack was located using X-ray radiography.

Next, a sequence of ELS tests was carried out (S.2a) with a loading angle +30°. The sequence consisted of a loading-unloading process at every displacement increment defined in Table 3. The loading and unloading rates were 2 mm/min and 5 mm/min, respectively. When the delamination front started to propagate, the loading velocity was slowed to 1 mm/min, and the displacement increment between cycles was set to 0.5 mm (Step S.2b). At the end of each displacement

increment, the specimen was released from the testing rig and the leading delamination front was inspected with X-ray radiography.

In the last step, the same method was repeated for the mode I test, setting the displacement increment at 1.5 mm, loading the specimen at 2 mm/min, and unloading it at 5 mm/min (step S.3). Again, the delamination process was inspected with X-ray radiography.

3.6. Hybrid static-fatigue loading sequence

The test configuration was replicated under a combination of static and fatigue loading. Two specimens were tested under the conditions specified in Table 4. The tests were performed in laboratory conditions at 23 ± 2 °C and at a RH of $50 \pm 5\%$. The step name nomenclature gives information regarding the loading is hybrid static-fatigue (H) and is followed by the boundary condition sequence number. The first step (H.1) consisted of a pre-crack DCB test. with a constant displacement rate of 5 mm/min until a crack length of $a_0 = 41$ mm was achieved.

Next, an ELS fatigue test was carried out under displacement control with the blocks rotated at an angle $\alpha = -30$. The fatigue loading sequence was initiated under sub-critical load. The applied maximum displacement was 7 mm, and the displacement ratio was $R_d = \delta_{min}/\delta_{max} = 0.1$ (Step H.2). The first 100 cycles were run at a test frequency of 1 Hz

Table 3
Loading conditions of the static test sequence:

Step	Loading mode	Loading angle, α [°]	Maximum displacement, δ_{max} [mm]	Displacement increment between loading-unloading cycles [mm]
S.1	Mode I	+0°	–	–
S.2a	Shear mode	+30°	10	1
S.2b	Shear mode	+30°	14.5	0.5
S.3	Mode I	−30°	25	1.5

Table 4
Loading conditions of the hybrid static-fatigue test sequence:

Step	Loading mode	Loading angle, α [°]	Maximum displacement, δ_{max} [mm]	Number of cycles
H.1	Mode I	+0°	–	- (static)
H.2	Shear mode	+30°	7	12 000
H.3a	Mode I	−30°	5	30 000
H.3b	Mode I	−30°	10	- (static)
H.3c	Mode I	−30°	10	400 000

to allow a smooth transition from mode I static loading to shear mode fatigue loading. For the rest of the cycles, the test frequency was 5 Hz. Stops were programmed at 200, 500, 1000, 2000, 3000, 4000, 5000, 6000, 7000, 8000, 10 000, 12 000 cycles, in which X-ray inspections of the delamination process were performed.

Then, sub-critical mode I fatigue loading was applied under displacement control at a maximum displacement of 5 mm and at a displacement ratio of $R_d = 0.1$ (Step H.3a). The frequency of the first 100 cycles was 1 Hz to allow a smooth transition from shear mode fatigue delamination to mode I fatigue loading. Setting a low frequency of 1 Hz was a precautionary measure to minimize a possible uncontrolled propagation of the process zone when changing the loading mode. Afterward, a test frequency of 5 Hz was set. The stops for X-ray monitoring were performed at 100, 200, 500, 1000, 5000, 15 000, 30 000 cycles.

After that, a static DCB test was carried out by loading the specimen under mode I loading at a constant loading rate of 2 mm/min until an opening displacement of 10 mm was reached (Step H.3b), keeping the same angle α like in the previous step (Step H.3a).

Finally, fatigue loading was applied under displacement control at a maximum displacement of 10 mm and a displacement ratio of $R_d = 0.1$ (Step H.3c). The maximum displacement was equal to the critical displacement applied in the previous step (H.3b). Like in the previous fatigue steps, the frequency of the first 100 cycles was set to 1 Hz, increasing the test frequency of 5 Hz for the rest of the test. The delamination process was inspected at 100, 200, 500, 1000, 5000, 15 000, 30 000, 100 000, and 400 000 cycles.

3.7. Post mortem fracture surface inspection

After the hybrid benchmark was tested, the fractured surfaces of the specimen were investigated by means of Scanning Electron Microscopy. The field emission scanning electron microscope Hitachi S4100 was used with a resolution of 3 nm at 20 kV. The specimens were opened "by hand". In this process, all the fibers bridging at the current damage process zone broke. However, SEM inspections were done on regions that were already completely separated beforehand opening. The samples were mounted on a 12 mm diameter aluminum sample holder stub with a double-adhesive carbon disc. A carbon coating was applied to the samples with an EMITECH K950 evaporator. Several points of the fractured surfaces of the different loading steps were inspected.

4. Benchmark test results

In this section, the results of both static and hybrid benchmark tests are presented: the load–displacement curves, the delamination process evolution data from the X-ray, and the SEM images of the fractured surfaces.
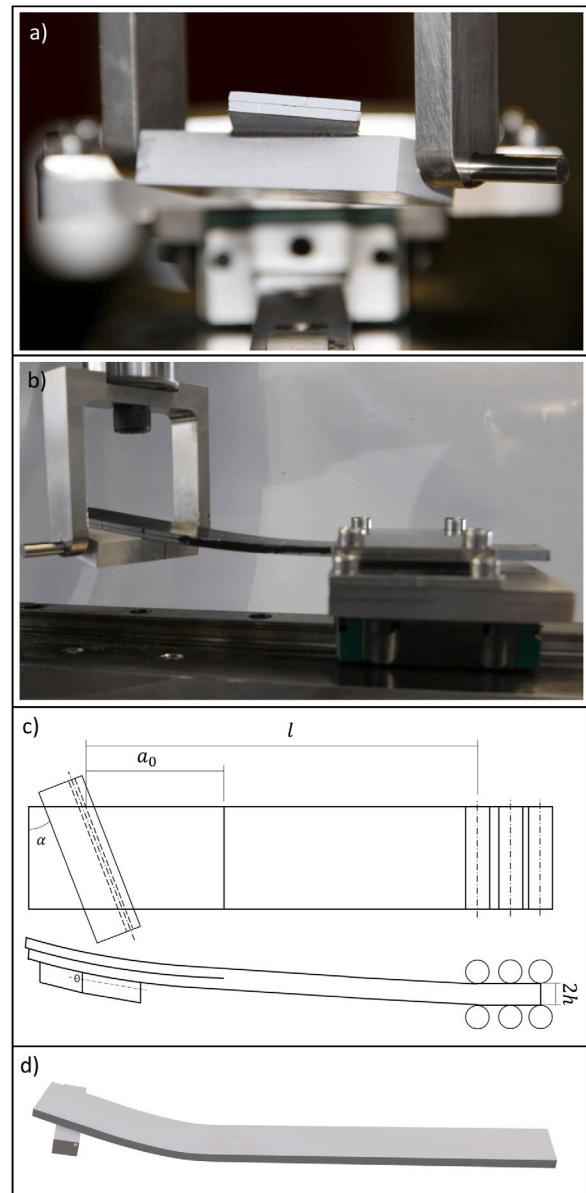

Fig. 4. (a) front and (b) lateral photographs of shear mode loading in the ELS test rig with the loading block inclined +30° (counter-clockwise direction) with respect to the longitudinal direction of the specimen. (c) 2D scheme of the top of the specimen, where a_0 is the initial delamination length at the start of the shear mode loading, l is the length of the specimen from the most distant loading point to the start of the clamping fixture, α is the loading block inclination with respect to the longitudinal direction of the specimen, and $2h$ is the total thickness of the specimen. (d) 3D scheme of the specimen.
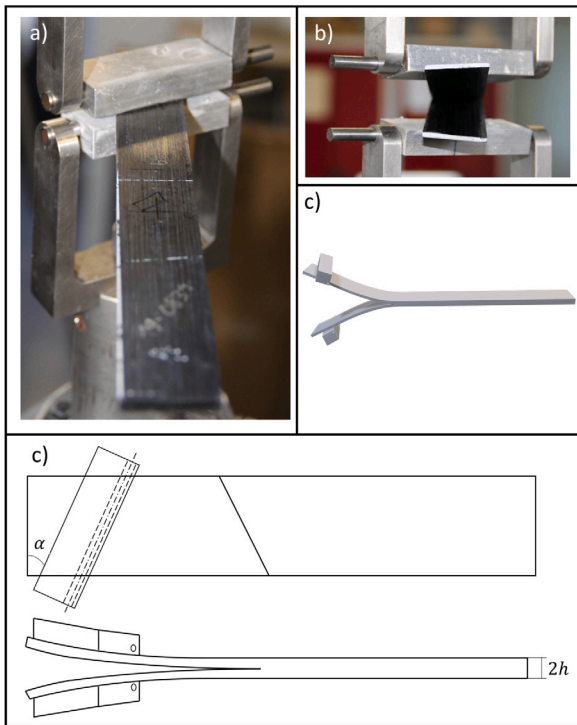
Fig. 5. Mode I loading in the DCB test rig with the loading block inclined −30° (clockwise direction) with respect to the longitudinal direction of the delamination plane.

Fig. 6. Load–displacement curves of the static ELS test (Steps S.2a and S.2b).

4.1. Static results

The results of each loading step of the static benchmark test are presented in the next subsection. The information on the boundary conditions applied in each step is included in Table 3.:

4.1.1. Step S.1: Static mode I loading, +0° loading angle

The first step was a quasi-static DCB with the block perpendicular to the crack propagation direction. The delamination process started from the insert at an initial crack length a_0 of 41 mm, and it was stopped after the delamination leading tip reached a distance of 56 mm from the loading block. In its wake, the presence of a damage process zone was detected. X-ray radiography was taken after the test (i.e. after unloading the specimen). The delamination state after mode I is plotted in Fig. 7 (first image on the top left, $d = 0$ mm), after post-processing the X-ray radiography data as specified in Section 3.3. The location of the leading delamination front is represented with black dots, while the detection of the wake of the damage process zone is illustrated with gray dots.

4.1.2. Step S.2a and S.2b: Static shear mode loading, +30° loading angle

After stopping the pre-cracking process, the loading blocks were rotated +30° (steps S2.a and S2.b). The test rig was changed to shear mode configuration (ELS test) as specified in Section 3.4.

In Fig. 6 the load–displacement curves resulting from the loading-unloading-inspection process of steps S.2a and S.2b are plotted. Each loading curve follows the unloading path of the previous curve until the onset of damage with a low amount of hysteresis, proving the consistency and repeatability of the inspection methodology. However, contrary to what it was expected, the non-linearity in a given loading path was onset at a lower value of force before reaching the maximum displacement of the previous loading path.

After each loading-unloading cycle X-ray radiography were obtained, Fig. 7 presents the leading delamination front (black dots)
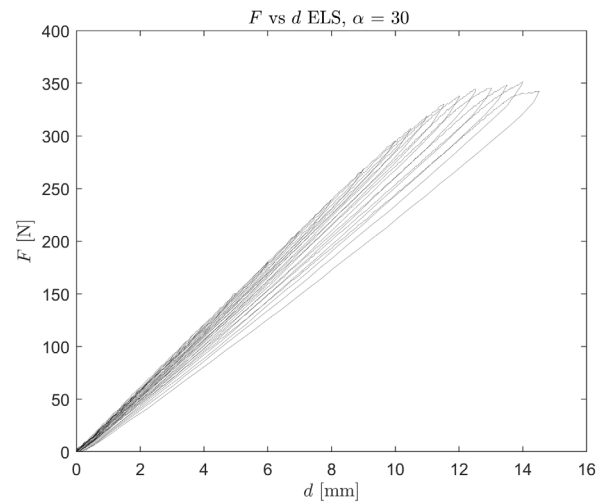
and the wake of the damage process zone (gray dots) detected. For comparison purposes, also the loading delamination tip after S.1 step is plotted. The results from $d = 4$ to $d = 10$ correspond to step S.2a and subsequent displacements to step S.2b. From $d = 0$ mm to $d = 9$ mm no delamination leading front propagation was observed from the X-ray radiography (static step S.2a). Moreover, within the 0–9 mm displacement range, the wake of the process zone remained the same. The results are in accordance with the force–displacement curves, where no deviations from the linear loading were observed in this range.

From $d = 10$ mm to $d = 14.5$ mm the crack front propagated at different rates along the specimen width, resulting in a rotation of the leading delamination front, which pivoted with respect to the left-hand-side following the inclination of the loading blocks (step S.2b). As the leading delamination front advanced, a new shear mode fracture surface was created (the area delimited by the black and blue dots). The wake of the damage process zone also moved. Instead, it was detected at the shear mode surface. The last image in Fig. 7 ($d = 14.5$ mm) shows a rotated crack front with an inclination towards the inclination of the block, but with a different angle, followed by the damage process zone wake located inside the new created fractured surface.

4.1.3. Step S.3: Static mode I loading, −30° loading angle

As shown in Table 3, in this step the loading block was inverted an angle of $\alpha = -30°$ by pure rotation of the loading blocks with respect to the middle point of the specimen width, and the test was switched to mode I loading configuration (DCB test). In Fig. 8 the load–displacement curves from the loading-unloading-inspection process of step S.3 are plotted. As in the case of Steps S.2a and S.2b, a low amount of hysteresis is observed, but the non-linearity started after $d = 6$ mm.

Due to the new loading block configuration and the inclination of the leading delamination front, the applied strain energy rate was maximum at the delamination point that was closest to the loading block (left-hand side of the specimen at Fig. 9, $d = 3$ mm). From $d = 0$ mm to $d = 12$ mm, the leading delamination front propagated at a higher rate at the points closer to the loading block. At $d = 6$ mm the wake of the process zone moved inside the fractured surface created by shear. However, after increasing the displacement to $d = 7.5$ mm, the wake of the process zone was located at the mode I delaminated surface. A perpendicular leading delamination front was obtained at $d = 12$ mm. Then the delamination leading front still propagated at different rates due to the inclined loading angle, resulting in a rotation of the crack front pivoting with respect to the right-hand-side crack tip point ($d = 12$ mm to $d = 24$ mm). The wake of the damage process zone was fixed and did not move.
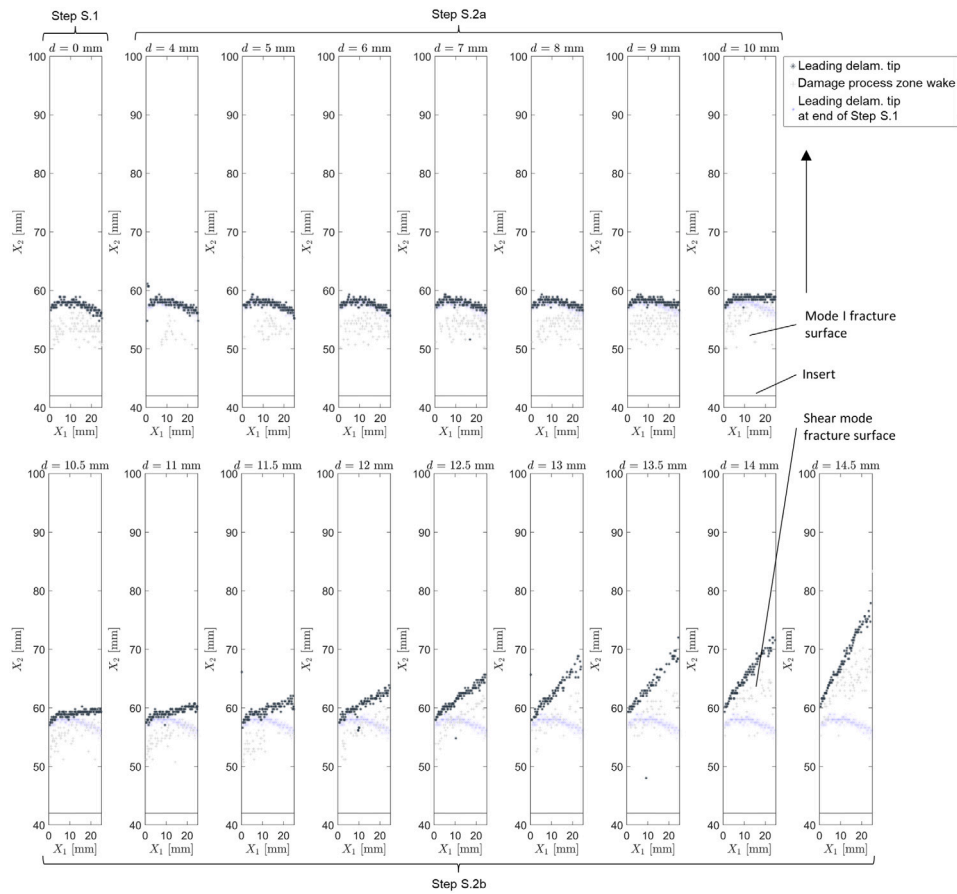
Fig. 7. Steps S1, S.2a and S.2b: Evolution of the delamination process under shear mode static loading monitored with X-ray radiography. X_1 is the specimen width, and X_2 is the specimen length from the load application point.
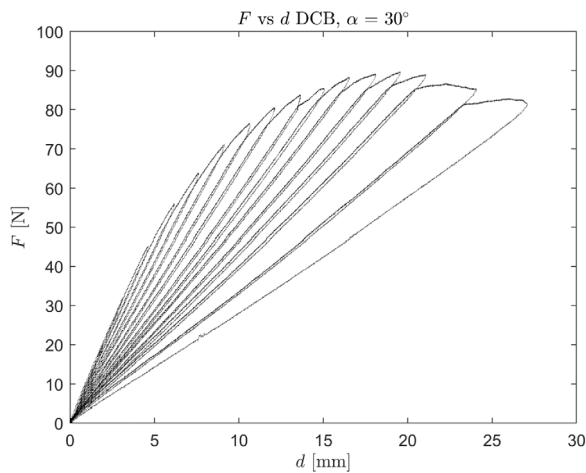

Fig. 8. Load–displacement curves of the static DCB test (Step S.3).

4.1.4. Overview of the static benchmark results

In Fig. 10 an overview of the delamination process is presented, where the most significant events regarding the delamination leading front and the wake of the damage process zone evolution during the static benchmark test are summarized.

4.2. Hybrid loading results

The results of each loading step of the hybrid benchmark test are described in the next subsections. The information of each load step is included in Table 4.:

4.2.1. Step H.1: Static mode I loading, +0° loading angle

The first step was a quasi-static DCB with the block perpendicular to the crack propagation direction. Fig. 11 shows the X-ray inspections done at each inspection period. $N = 0$ mm represents the state after the static mode I pre-cracking procedure. The pre-cracking was initiated from an insert with an initial crack length a_0 measuring 41 mm, then propagation of the leading front until a crack length of 56 mm was followed, developing a static damage process zone.

4.2.2. Step H.2: Fatigue shear mode loading, +30° loading angle

Following the pre-cracking procedure, the loading blocks were rotated an angle $\alpha = +30°$. This rotation positioned the farthest point of the loading block at a distance of 56 mm from the former delamination front. An ELS fatigue test was carried out.

The fatigue test was conducted under displacement control shear mode cyclic loading with a maximum displacement of 7 mm and displacement ratio $R = 0.1$, having sub-critical shear mode loading. The cyclic test was carried out during 12 000 cycles. The monitored delamination evolution with X-ray radiography is plotted in Fig. 11. After 500 cycles, the wake of the process zone inside the mode I fracture surface was no longer detected. During the shear fatigue test (Step H.2) the delamination evolved analogous to the static loading (Step S.2a and S.2b). At the end of the shear fatigue test, an inclined leading delamination front was found, and a shear mode fracture surface was generated. A process zone wake was detected inside the shear mode fracture surface after 3000 cycles. A high repeatability between both tested specimens was observed.

4.2.3. Step H.3a: Fatigue mode I loading, −30° loading angle

In this step a mode I DCB fatigue test was performed and the loading block angle was rotated from +30° to −30°. A displacement control
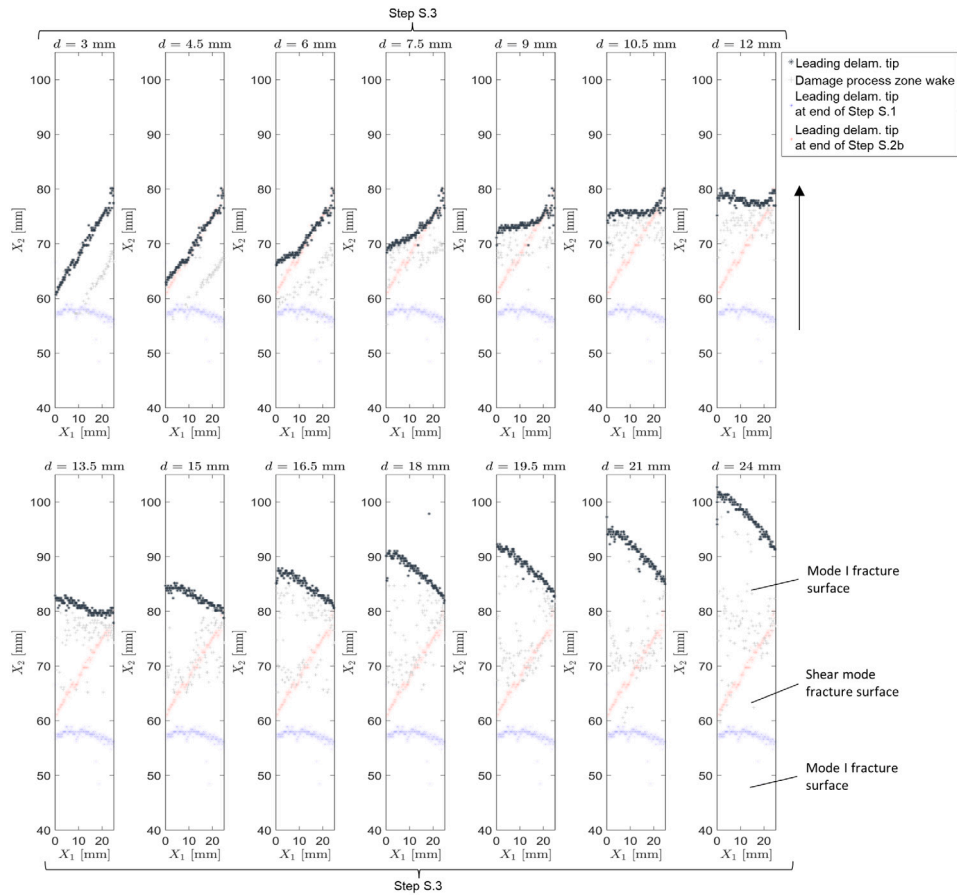
Fig. 9. Step S.3: Evolution of the delamination process under mode I static loading monitored with X-ray radiography.
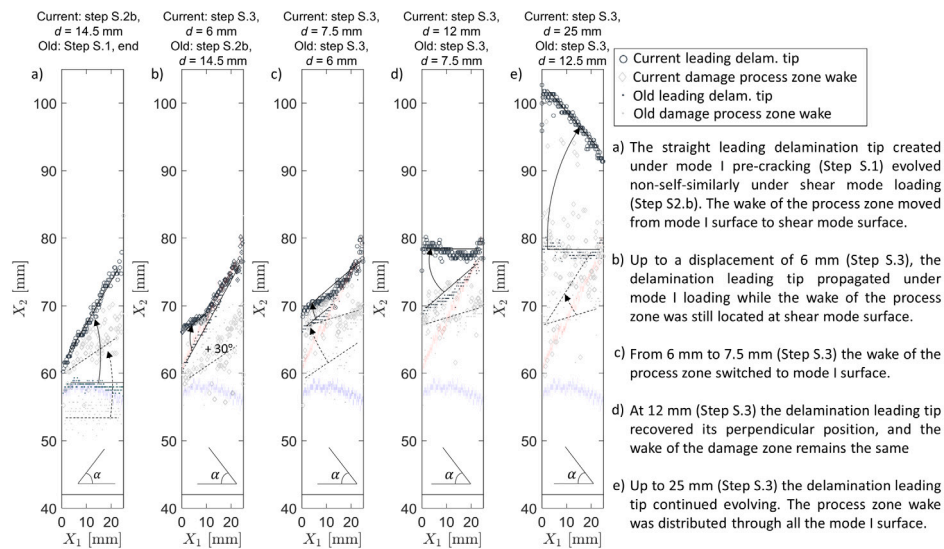

Fig. 10. Overview of the static benchmark results, where α is the inclination of the block.

test at a maximum displacement of 5 mm and R = 0.1 was carried out, resulting in a sub-critical fatigue loading test. The delamination evolution is reported in Fig. 12. In total 30 000 cycles were applied, in which the inclined leading delamination front kept rotating, positioning

it perpendicular to the longitudinal axis of the specimen due to the loading block angle configuration. A total divergence of about 4 mm at the left-hand side of the leading delamination front was observed between the two tested specimens. However, the same response in both
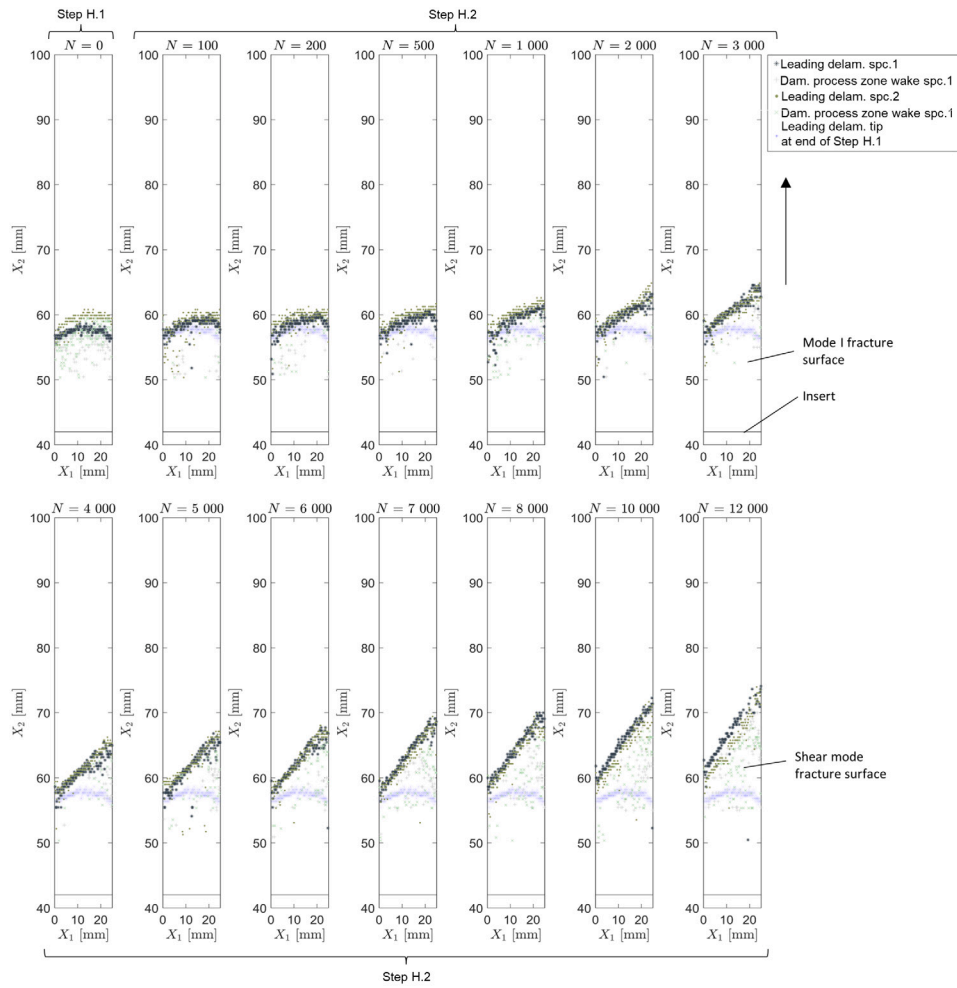
Fig. 11. Step H.1 and H.2: Evolution of the delamination process under shear mode fatigue loading at a maximum displacement of 7 mm monitored with X-ray radiography fore the two specimens tested (spc.1 and spc.2).
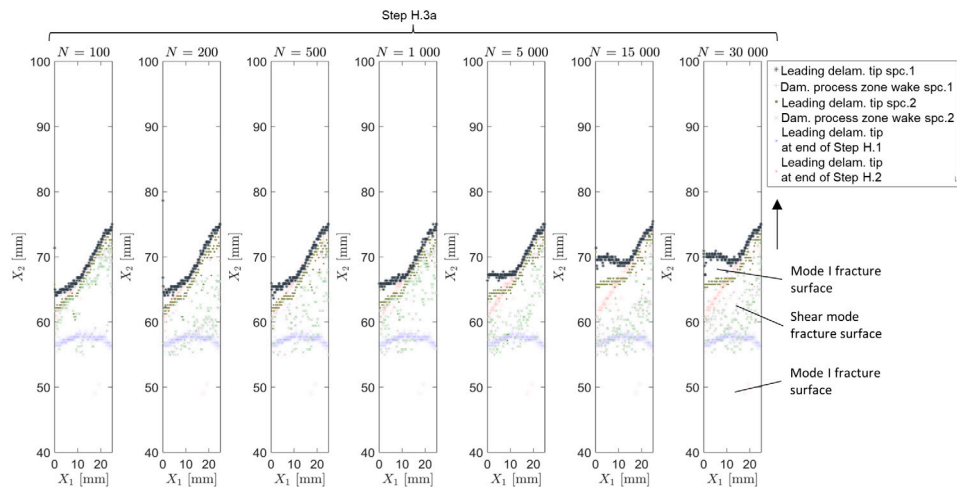

Fig. 12. Steps H.3a and H.3b: Evolution of the delamination process under mode I fatigue loading at a maximum displacement of 5 mm monitored with X-ray radiography.

specimens was monitored. Despite the fact that mode I delamination was promoted, the shear mode process zone did not move during mode I fatigue loading. This is in agreement with the static delamination results (Step S.2a), where a mode I static loading of 5 mm did not erase the shear mode process zone (Fig. 7).

4.2.4. Step H.3b: Static mode I loading, −30° loading angle

After the sub-critical mode I fatigue, static delamination was promoted by statically increasing the maximum displacement from 5 mm to 10 mm. The delamination front after the static loading is plotted in Fig. 13, $N = 0$. As a consequence of the increased displacement,
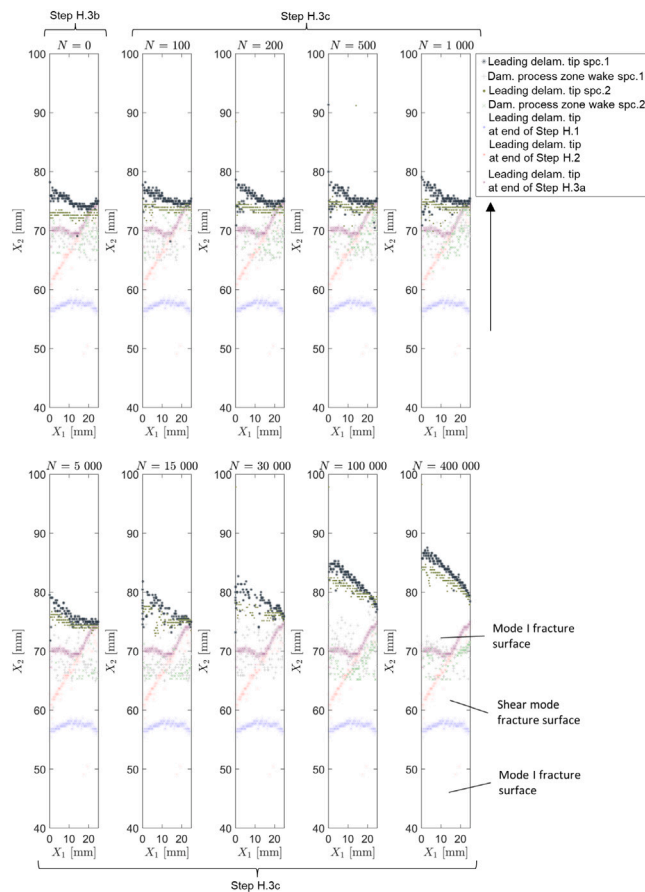
Fig. 13. Step H.3C: Evolution of the delamination process under mode I fatigue loading at a maximum displacement of 10 mm monitored with X-ray radiography.

the leading delamination front evolved, locating perpendicular to the longitudinal direction of the specimen. Moreover, the process zone formerly observed at the shear mode surface propagated, advancing the wake of the FPZ to the mode I fracture surface.

4.2.5. Step H.3c: Fatigue mode I loading, −30° loading angle

Next, a mode I fatigue test controlled by displacement, with d_{max} = 10 mm and R = 0.1 was carried out. The fatigue test was ended after 400 000 cycles. Images of the damage evolution at different stages (i.e. cycles) are plotted in Fig. 13. The crack front advanced at different propagation rates causing the front to pivot and rotate with respect to the delamination tip point located at the right-hand side of the specimen. The detected process zone wake did not propagate during this step.

4.2.6. Overview of the hybrid benchmark results

In Fig. 14, an overview of the delamination process is presented, where the most significant events regarding the delamination leading front and the wake of the damage process zone evolution during the hybrid benchmark test are summarized.

4.3. Post mortem fracture surface inspection results

After the testing, the fracture surfaces were inspected with the SEM technique. One spot in the mode I pre-crack region (1), three spots in the shear mode fracture surface (2, 3, 4), and three spots in the mode I fracture surface (5, 6, 7) were analyzed (Fig. 15). At inspection spots 3, 4, and 5, several widths of the specimen were targeted, looking for evidence in the traces of the damage mechanisms regarding (a) the

influence of mode III component and (b) traces of both mode I and shear mode at material points where both loading modes were applied. At each inspection spot, images with 200 and 1000 magnifications were taken.

Regarding the mode I pre-cracked surface spot, matrix traces and small cut fibers without adhered matrix were observed (Fig. 16a). The SEM images of the shear mode fracture surface evidenced rounded shear cusps on the matrix-rich regions and a large amount of matrix plastic deformation between the fiber imprints forming striations (Fig. 16b,c,d) [46]. Regarding the SEM images corresponding to mode I loading, single fiber bridges and fiber bundle bridges were observed. Matrix particles were found to adhere to the fibers, showing good fiber/matrix bonding and evidencing plastic strain before fracture (Fig. 17).

5. Discussion of the results

In this section, the information obtained from the X-ray data on the non-self-similar delamination evolution is complemented with the SEM observations of the fracture surfaces. An attempt is made to provide a physical understanding of the role of the failure mechanisms as a function of the test boundary conditions in a non-self-similar delamination process.

5.1. Correlation between fracture surface inspection and detected wake of the damage process zone

During the X-ray inspections, a point was set to be the wake of the damage process zone if the calculated attenuation signal slope of the moving linear regression abruptly deviated from the continuous trend as well as the R^2 of the regression decreased significantly (Fig. 3). Considering the SEM images, a correlation between the traces of damage mechanisms in the *post mortem* fracture surfaces and the damage process zone detected in X-ray inspections could be done. In the fracture surfaces created under mode I loading (Figs. 9, 12 and 13), the detected process zone was correlated with fiber bridging (Fig. 17), and in the fracture surfaces created under shear mode loading (Figs. 7 and 11), it was correlated with the merging of micro-cracks and a matrix plastic strain (Fig. 16c). The detection of the wake of the damage process zone is not homogeneous because the mechanisms that constitute it, such as bridging or plasticity, are also not homogeneous either.

5.2. Contribution of the mode I process zone to shear mode loading

A process zone was detected in the X-ray images after the pre-cracking of the specimens (Fig. 11). In the case of the hybrid benchmark test, the detected process zone in the mode I pre-crack surface was swapped away during the first 500 cycles of fatigue shear mode loading, Fig. 11, (N = 0 to N = 500). The SEM micrographs of this spot show matrix traces and fragments of small fibers (inspection spot 1, Fig. 16a). It can be argued that these observations could have been formed from a standard mode I loading fracture surface (Fig. 17c) where fiber bridges with matrix traces attached to them ended up being cut into small parts due to friction between delaminated surfaces during shear mode fatigue loading. It is hypothesized that this may indicate that the contribution of a mode I process zone could have a limited contribution to shear mode fatigue resistance under cyclic loading.

In the static benchmark test, the damage process zone at the mode I pre-crack region was detected until the leading delamination front began to propagate under shear mode loading (Fig. 7, d = 10 mm). Up to this point, the X-ray detection events were attributed to fiber bridging created during the mode I pre-crack. When the shear separation onset and increased due to shear loading, the damage process zone was no longer detected at the mode I pre-crack zone. The mode I process zone energy dissipation is dominated mainly by fiber bridging breakage, and
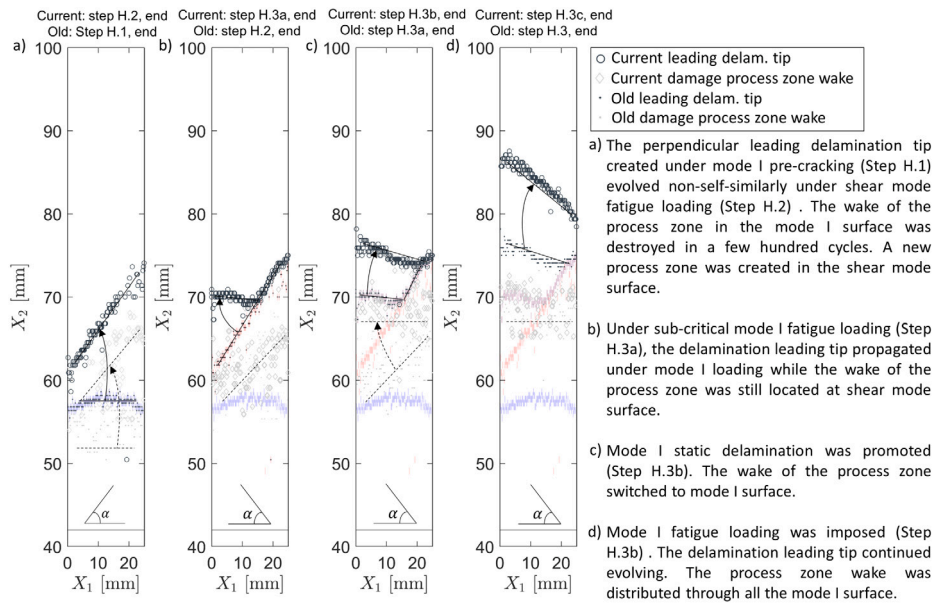
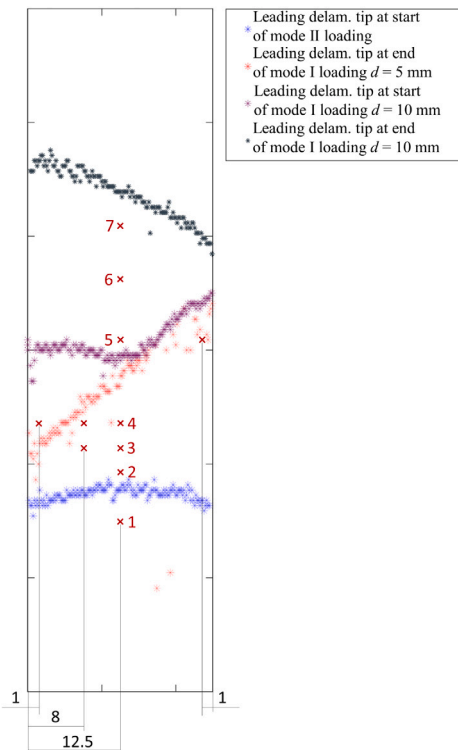**Fig. 14.** Overview of the fatigue benchmark results.

Fig. 15. Location of the SEM *post mortem* fracture surface inspection spots.

the matrix in the mode I process zone can be considered completely damaged (Fig. 17b). Therefore, the mode I process zone fiber bridges seem to contribute to the strength of the interface until the material that was not damaged under mode I loading gets completely damaged under shear loading, generating shear mode delamination. From that point, the shear mode separations at the mode I fractured process zone will increase, and fibers will fail due to fiber breakage under compression stresses and fiber pull out [47]. It can therefore be argued that the mode I process zone contributes to the shear delamination resistance under static loading until the fiber bridging breaks.

5.3. Contribution of a shear mode process zone to mode I loading

After the shear mode loading, an inclined leading delamination front followed by a process zone was observed (Figs. 9 and 12). The SEM observations confirmed that the process zone detected in the shear mode fracture surface had the usually reported damage mechanisms such as shear cusps and striations, which are indicative of a shear mode process zone with merging micro-cracks and a matrix plastic strain (Fig. 16c). For the case of the static benchmark test, a damage process zone at the shear mode surface was still detected even after the crack started to propagate under mode I loading. Shear mode damage mechanisms were detected at a displacement of $d = 6$ mm. Once reaching a maximum mode I displacement of $d = 7.5$ mm, the process zone was no longer detected in the shear mode fracture surface (Fig. 9). This may indicate that the process zone formed under shear mode loading contributed to mode I delamination resistance under static loading. This contribution ceased until a critical value of mode I separation was imposed in the process zone. It can be argued that, since the energy is mainly dissipated by the matrix under shear mode loading, the remaining shear mode process zone that is not completely damaged still has potential fiber bridges and a matrix portion to contribute to the mode I separation resistance. However, it must also be mentioned that the process zone formed during shear mode loading (formation of shear cusps and striations) is re-arranged to withstand mode I loading. Therefore, when reaching a certain imposed mode I separation, the shear mode process zone that is still active fails at a lower available strain energy release rate than the mode I process zone.

As the mode I delamination process continued, a process zone was created at the mode I fracture surface (Fig. 9), which was related to fiber bridging (Fig. 17). As the leading delamination front propagated, the wake of the process zone did not, being indicative of the development of large-scale fiber bridging.

With regards to fatigue, when a sub-critical mode I cyclic displacement of 5 mm was applied, the damage process zone was still detected at the shear mode fractured surface, even after mode I fatigue delamination occurred after 30 000 cycles (Fig. 12). As it can be seen in Fig. 9, for a static mode I loading below 7.5 mm of displacement did not completely damage the static shear mode process zone. These results indicated that a shear mode process zone might contribute to the fatigue performance of a structure under mode I fatigue loading if the applied displacement is below the critical mode I static separation that completely damages the shear mode FPZ.
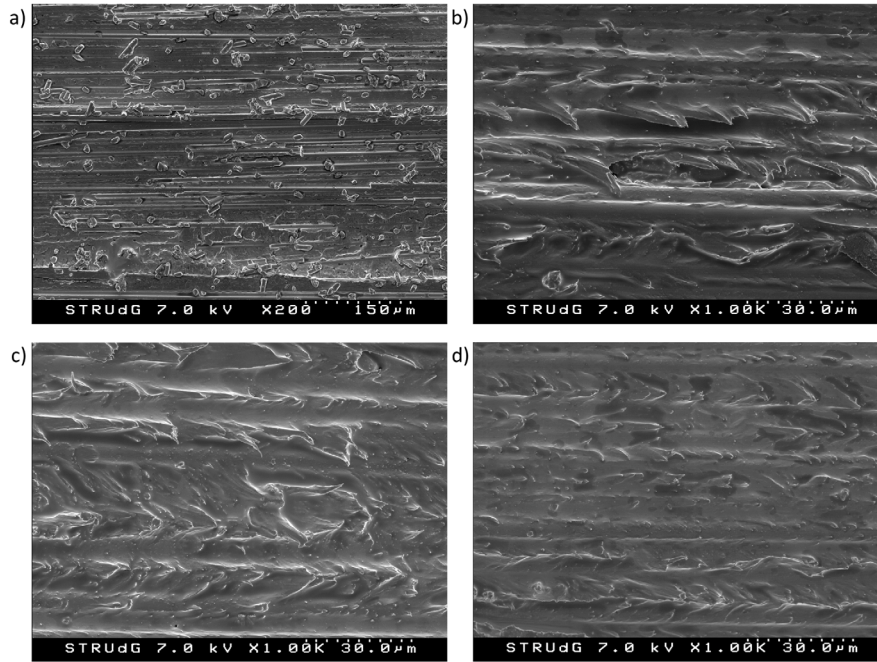
Fig. 16. SEM image of (a) spot 1, mode I pre-crack, 12.5 mm width, x200, (b) spot 2, shear mode, 12.5 mm width, x1000, (c) spot 3, shear mode, 12.5 mm width, x1000, and (d) spot 4, shear mode, 12.5 mm width, x1000.
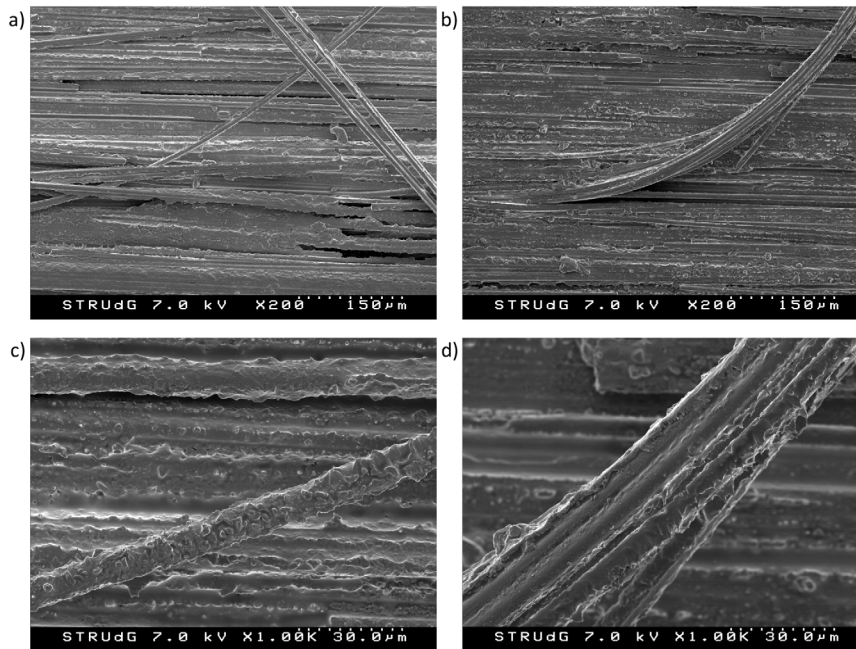

Fig. 17. SEM image of (a) spot 5, mode I, 12.5 mm width, x200, (b) spot 7, mode I, 12.5 mm width, x200, (c) spot 6, mode I, 12.5 mm width, x1000, and (d) spot 7, mode I, 12.5 mm width, x1000.

Then, in the hybrid static-fatigue test, the mode I displacement was statically increased to 10 mm, Fig. 13. The shear mode process zone was completely damaged, so the damage process zone was only detected in the mode I fracture surface. The damage zone after the static loading was correlated with fiber bridging (Fig. 17).

5.4. Fracture surface at material points that withstood both pure mode I and shear mode loading

No evidence of both mode I and shear mode loading were found at material points where first fatigue shear mode and then mode I
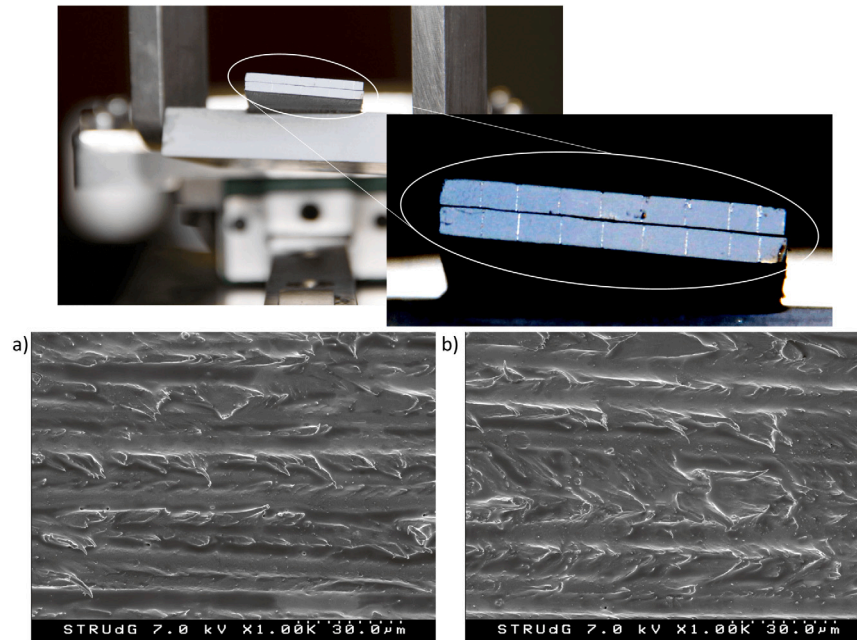
Fig. 18. Evidence of mode III component in shear mode loading configuration. SEM image of (a) spot 3, shear mode, 8 mm width, x1000, (b) spot 3, shear mode, 12.5 mm width, x1000.

were applied. This can be attributed to the fact that both shear cusps and striations may be extensions of micro-cracks (Fig. 16c). According to [46], shear cusps are formed from micro-cracks created in resin-rich areas, and striations of plastic strain are a consequence of the micro-cracks that propagate around the fibers. Therefore, even certain amount of shear mode damage was induced, micro-cracks may not have fully developed at partially shear mode damaged regions and therefore did not leave the characteristic imprint on the SEM images.

5.5. Influence of the available strain energy release rate in the fatigue process zone evolution

It is worth noting that the plastic deformation traces at shear mode fracture regions were sharper and with longer "branches", and also the shear cusps more pronounced in Fig. 16b compared to Fig. 16c and d, and in Fig. 16c compared to Fig. 16d (plastic deformation traces in inspection spots 2 > 3 > 4). This may be because the shear mode openings were higher at fracture surfaces created at higher severities. Therefore, in the fracture surfaces created at higher severity, plastic strain that requires higher energetic thresholds could be released compared to fracture surfaces created at lower severity. Regarding the SEM images corresponding to mode I loading, Fig. 17, the matrix adhered to the fibers had a more round shape compared to the static mode I micrography of the AS4D/PEKK-FC thermoplastic composite presented in [20], where a harsh shape was present. This indicates that a higher amount of plastic strain is developed under static mode I delamination than under fatigue mode I loading. This is in agreement with the observations made in [30,48], where they correlated the available strain energy release rate during fatigue loading with the activation of different damage mechanisms. This could be understood as that under higher severity cyclic loading there is energy enough to activate certain damage thresholds and propagate at higher rate, while in process zones under lower severities, the damage mechanisms are not activated and more cycles are needed to create a free surface, resulting in lower propagation rates. The observation suggests that the static characterization of the $\mathcal{R}$-curve may not accurately reflect the fatigue process zone

evolution of a material since the plastic energy dissipation mechanism may be a function of the available energy release rate during fatigue loading.

5.6. Contribution of the mode III loading component to the shear mode fracture surface

Due to the loading block configuration, a mode III component was introduced during the shear mode loading test (Fig. 18). However, the specific contribution of the mode III component to the delamination process could not be clearly distinguished from the mode II component among delaminated regions under shear mode loading. Due to the way the delamination front evolved during the shear mode test configuration, it was expected the mode III to have a higher contribution in the SEM spot 3, 12.5 mm width (Fig. 18b) compared to spot 4, 8 mm width (Fig. 18a). However, this could not be clearly observed in the SEM images. It could be because the fractographic events of mode III loading compared to mode II loading are so similar that cannot be distinguished.

This information is crucial for accurate modeling of in-service structures. If complex loading conditions want to be considered in potentially non-self-similar delamination scenarios, the contribution of the $\mathcal{R}$-curve of the material as a function of the nature of the applied load (static or fatigue) and loading mode history must be taken into account.

6. Conclusions

The main contribution of this work is to present a novel benchmark test concept for composite materials, which allows more complex load cases to be analyzed rather than straight crack fronts. A non-self-similar delamination is promoted in standardized test specimens, achieving a compromise between testing complexity and rich phenomenological delamination data. The test allows analyzing the effect of loading mode history under static and fatigue loading in a single specimen. The benchmark test concept introduced in this paper can be particularized

for any given composite material set and any sequence of loading conditions.

To illustrate the capabilities of the benchmark test, a case study was provided for AS4D/PEKK-FC thermoplastic composite material, which is known to have a strong $\mathcal{R}$-curve behavior. A given sequence of loading conditions were applied under static and fatigue loading, and the evolution of the delamination process was monitored with X-ray radiography. The case study can be seen as an additional contribution in itself, providing an experimental data set that can be used as part of the validation process for numerical predictive delamination models. This is a step towards ensuring that the delamination models properly account for the failure mechanisms acting during the delamination process, and to allow a hybrid numerical-experimental building block approach. However, the effects of fiber orientation, variation in lay-up sequence, two-dimensional delamination propagation, and the interactions between multiple delamination sites [49–53], among others, must also be considered before fully validating a delamination model to predict the behavior of a component or a structure.

Moreover, the X-ray detection of the process zone wake was correlated with SEM images of the *post mortem* fracture surfaces, allowing to formulate of a series of hypotheses regarding the physics behind fatigue delamination, the relevance of the damage process zones, and their contribution to fatigue resistance under complex loading:

- In the fracture surfaces created under mode I loading, the detected process zone was correlated with fiber bridging, and in the fracture surfaces created under shear mode loading, it was correlated with the merging of micro-cracks and a matrix plastic strain.
- The contribution of a mode I process zone could have a limited contribution to shear mode fatigue resistance under cyclic loading, but it could contribute to the shear delamination resistance under static loading until the fiber bridging breaks.
- The shear mode process zone might have potential fibers and a matrix portion to contribute to the mode I separation resistance until reaching a certain imposed mode I separation, where it fails at a lower available strain energy release rate than the mode I process zone. Under fatigue loading, it may also contribute to the fatigue performance of a structure under mode I loading if the applied displacement is below the critical mode I static separation that completely damages the shear mode FPZ.
- No evidence of both mode I and shear mode loading were found at material points where first fatigue shear mode and then mode I were applied.
- The static characterization of the $\mathcal{R}$-curve may not accurately reflect the fatigue process zone evolution since the plastic energy dissipation mechanism may be a function of the available energy release rate during fatigue loading.
- The specific contribution of the mode III component to the delamination process could not be clearly distinguished from the mode II component among delaminated regions under shear mode loading.

It was concluded that the loading mode history must be considered in materials that exhibit $\mathcal{R}$-curve effects to accurately model the delamination process of an in-service structure.

CRediT authorship contribution statement

I. Leciñana: Conceptualization, Investigation, Methodology, Software, Writing – original draft. **J. Renart:** Conceptualization, Investigation, Methodology, Resources, Writing – review & editing, Supervision. **L. Carreras:** Conceptualization, Investigation, Methodology, Resources, Supervision, Writing – review & editing. **A. Turon:** Conceptualization, Methodology, Resources, Supervision, Writing – review & editing. **J. Zurbitu:** Conceptualization, Resources, Supervision, Writing – review & editing. **B.H.A.H. Tijs:** Conceptualization, Resources, Supervision, Writing – review & editing.

Declaration of competing interest

The authors declare the following financial interests/personal relationships which may be considered as potential competing interests: J. Renart reports financial support was provided by Spanish Government. A. Turon reports financial support was provided by Government of Catalonia. L. Carreras reports financial support was provided by European Union. B.H.A.H. Tijs reports financial support was provided by European Union. I. Lecinana has patent pending to EP23382498. L. Carreras has patent pending to EP23382498. A. Turon has patent pending to EP23382498. J. Renart has patent pending to EP23382498. J. Zurbitu has patent pending to EP23382498.

Data availability

The processed data required to reproduce these findings are available to download from doi: http://dx.doi.org/10.17632/jbr6zytdps.1, an open-source online data repository hosted at Mendeley Data.

References

[1] Federal Aviation Autority F. Airworthiness advisory circular no: 20-107B. 2009, Code of Federal Regulations (14 CFR).

[2] Department of Defense Standard Practice: ASIP M-S. MIL-STD-1530D (2016). Program 2016;(February 2004).

[3] Jones R, Peng D, Michopoulos JG, Kinloch AJ. Requirements and variability affecting the durability of bonded joints. Materials 2020;13(6):1–23. http://dx.doi.org/10.3390/ma13061468.

[4] Hojo M, Gustafson C, Tanaka K, Hayashi R. Mode I propagation of delamination fatigue cracks in CFRP. In: Advanced materials for severe service applications. 1990, p. 353–72. http://dx.doi.org/10.1007/978-94-009-3445-0_23.

[5] Brunner AJ, Murphy N, Pinter G. Development of a standardized procedure for the characterization of interlaminar delamination propagation in advanced composites under fatigue mode I loading conditions. Eng Fract Mech 2009;76(18):2678–89. http://dx.doi.org/10.1016/j.engfracmech.2009.07.014.

[6] Stelzer S, Brunner AJ, Argüelles A, Murphy N, Pinter G. Mode I delamination fatigue crack growth in unidirectional fiber reinforced composites: Development of a standardized test procedure. Compos Sci Technol 2012;72(10):1102–7. http://dx.doi.org/10.1016/j.compscitech.2011.11.033.

[7] Stelzer S, Brunner AJ, Argüelles A, Murphy N, Cano GM, Pinter G. Mode I delamination fatigue crack growth in unidirectional fiber reinforced composites: Results from ESIS TC4 round-robins. Eng Fract Mech 2014;116:92–107. http://dx.doi.org/10.1016/j.engfracmech.2013.12.002.

[8] Brunner A, Stelzer S, Pinter G, Terrasi G. Mode II fatigue delamination resistance of advanced fiber-reinforced polymer–matrix laminates: Towards the development of a standardized test procedure. Int J Fatigue 2012. http://dx.doi.org/10.1016/j.ijfatigue.2012.02.021.

[9] Murri GB. Effect of data reduction and fiber-bridging on Mode i delamination characterization of unidirectional composites. J Compos Mater 2014;48(19):2413–24. http://dx.doi.org/10.1177/0021998313498791.

[10] Bak BLV, Sarrado C, Turon A, Costa J. Delamination under fatigue loads in composite laminates : A review on the observed phenomenology and computational methods. Appl Mech Rev 2014;66(6). http://dx.doi.org/10.1115/1.4027647.

[11] Alderliesten RC, Brunner AJ, Pascoe JA. Cyclic fatigue fracture of composites: What has testing revealed about the physics of the processes so far? Eng Fract Mech 2018;203(June):186–96. http://dx.doi.org/10.1016/j.engfracmech.2018.06.023.

[12] Pérez-Galmés M, Renart J, Sarrado C, Brunner AJ, Rodríguez-Bellido A. Towards a consensus on mode II adhesive fracture testing: Experimental study. Theor Appl Fract Mech 2018;98:210–9. http://dx.doi.org/10.1016/j.tafmec.2018.09.014.

[13] ASTM Standards. ASTM D5528/D5528M-21: Standard test method for mode I interlaminar fracture toughness of unidirectional fiber-reinforced polymer matrix composites. Book Stand 2021;15.03. http://dx.doi.org/10.1520/D5528_D5528M-21.

[14] ASTM International. ASTM D6115-97(2004), standard test method for mode I fatigue delamination growth onset of unidirectional fiber-reinforced polymer matrix composites. 2004, http://dx.doi.org/10.1520/D6115-97R19, URL: www.astm.org.

[15] ISO Standards. ISO 15114:2014 Fibre-reinforced plastic composites — Determination of the mode II fracture resistance for unidirectionally reinforced materials using the calibrated end-loaded split (C-ELS) test and an effective crack length approach. 2014.

[16] Turon A, Costa J, Camanho PP, Dávila CG. Simulation of delamination in composites under high-cycle fatigue. Composites A 2007;38(11):2270–82. http://dx.doi.org/10.1016/j.compositesa.2006.11.009.

[17] Pirondi A, Moroni F. Simulation of mixed-mode I/II fatigue crack propagation in adhesive joints with a modified cohesive zone model. J Adhes Sci Technol 2011;25(18):2483–99. http://dx.doi.org/10.1163/016942411X580180.

[18] Harper PW, Hallett SR. A fatigue degradation law for cohesive interface elements - Development and application to composite materials. Int J Fatigue 2010;32(11):1774–87. http://dx.doi.org/10.1016/j.ijfatigue.2010.04.006.

[19] Bak BLV, Turon A, Lindgaard E, Lund E. A benchmark study of simulation methods for high-cycle fatigue-driven delamination based on cohesive zone models. Compos Struct 2017;164:198–206. http://dx.doi.org/10.1016/j.compstruct.2016.11.081.

[20] Tijs BH, Abdel-Monsef S, Renart J, Turon A, Bisagni C. Characterization and analysis of the interlaminar behavior of thermoplastic composites considering fiber bridging and R-curve effects. Composites A 2022;162:107101. http://dx.doi.org/10.1016/j.compositesa.2022.107101.

[21] Lecinana I, Renart J, Turon A, Zurbitu J, Tijs B. Characterization and analysis of the mode I interlaminar fatigue behaviour of thermoplastic composites considering R-curve effects. Eng Fract Mech 2023;286(June). http://dx.doi.org/10.1016/j.engfracmech.2023.109273.

[22] Carreras L, Renart J, Turon A, Costa J, Bak BLV, Lindgaard E, Martin de la Escalera F, Essa Y. A benchmark test for validating 3D simulation methods for delamination growth under quasi-static and fatigue loading. Compos Struct 2019;210(October 2018):932–41. http://dx.doi.org/10.1016/j.compstruct.2018.12.008.

[23] Manterola J, Aguirre M, Zurbitu J, Renart J, Turon A, Urresti I. Using acoustic emissions (AE) to monitor mode I crack growth in bonded joints. Eng Fract Mech 2020;224(October 2019):106778. http://dx.doi.org/10.1016/j.engfracmech.2019.106778.

[24] Carreras L, Bak BLV, Jensen S, Lequesne C, Xiong H, Lindgaard E. Benchmark test for mode I fatigue-driven delamination in GFRP composite laminates: Experimental results and simulation with the inter-laminar damage model implemented in SAMCEF. Composites B 2023;253(December 2022):110529. http://dx.doi.org/10.1016/j.compositesb.2023.110529.

[25] Clay SB, Knoth PM. Experimental results of quasi-static testing for calibration and validation of composite progressive damage analysis methods. J Compos Mater 2017;51(10):1333–53. http://dx.doi.org/10.1177/0021998316658539.

[26] Jensen SM, Bak BLV, Bender JJ, Lindgaard E. Transition-behaviours in fatigue-driven delamination of GFRP laminates following step changes in block amplitude loading. Int J Fatigue 2021;144(June 2020):106045. http://dx.doi.org/10.1016/j.ijfatigue.2020.106045.

[27] Jensen SM, Bak BLV, Bender JJ, Carreras L, Lindgaard E. Transient delamination growth in GFRP laminates with fibre bridging under variable amplitude loading in G-control. Composites B 2021;225(September):109296. http://dx.doi.org/10.1016/j.compositesb.2021.109296.

[28] Bender JJ, Bak BLV, Jensen SM, Lindgaard E. Effect of variable amplitude block loading on intralaminar crack initiation and propagation in multidirectional GFRP laminate. Composites B 2021;217(December 2020):108905. http://dx.doi.org/10.1016/j.compositesb.2021.108905.

[29] Bender JJ, Bak BLV, Carerras L, Lindgaard E. Intralaminar crack growth rates of a glass fibre multiaxial laminate subjected to variable amplitude loading. Composites B 2023;252(December 2022):110510. http://dx.doi.org/10.1016/j.compositesb.2023.110510.

[30] Ferreira Motta R, Alderliesten R, Zarouchas D, Yutaka Shiino M, Odila Hilario Cioffi M, Jacobus Cornelis Voorwald H. Explaining the multiple energy thresholds for damage mechanisms activation in laminate composites under cyclic loadings. Composites A 2023;167(September 2022). http://dx.doi.org/10.1016/j.compositesa.2023.107451.

[31] Greenhalgh ES. Failure analysis and fractography of polymer composites. 2009, p. 595. http://dx.doi.org/10.1533/9781845696818.

[32] Amaral L, Alderliesten R, Benedictus R. Understanding mixed-mode cyclic fatigue delamination growth in unidirectional composites: An experimental approach. Eng Fract Mech 2017;180:161–78. http://dx.doi.org/10.1016/j.engfracmech.2017.05.049.

[33] Daneshjoo Z, Amaral L, Alderliesten RC, Shokrieh MM, Fakoor M. Development of a physics-based theory for mixed mode I/II delamination onset in orthotropic laminates. Theor Appl Fract Mech 2019;103(March):102303. http://dx.doi.org/10.1016/j.tafmec.2019.102303.

[34] Jaeck I, Carreras L, Renart J, Turon A, Martin de la Escalera F, Essa Y. Experimental methodology for obtaining fatigue crack growth rate curves in mixed-mode I-II by means of variable cyclic displacement tests. Int J Fatigue 2018;110(January):63–70. http://dx.doi.org/10.1016/j.ijfatigue.2018.01.016.

[35] ASTM Standards. ASTM D6671M-22: Standard test method for mixed mode I-mode II interlaminar fracture toughness of unidirectional fiber reinforced polymer matrix composites. 2022, p. 15. http://dx.doi.org/10.1520/D6671_D6671M-22.

[36] Davies P, Sims GD, Blackman BRK, Brunner aJ, Kageyama K, Hojo M, Tanaka K, Murri G, Rousseau C, Gieseke B, Martin RH. Comparison of test configurations for the determination of GIIC: Results from an international round robin. Plast Rubber Compos 1999;28(September):432–7.

[37] Daneshjoo Z, Shokrieh MM, Fakoor M. A micromechanical model for prediction of mixed mode I/II delamination of laminated composites considering fiber bridging effects. Theor Appl Fract Mech 2018;94(January):46–56. http://dx.doi.org/10.1016/j.tafmec.2017.12.002.

[38] Gong Y, Zhao L, Zhang J, Wang Y, Hu N. Delamination propagation criterion including the effect of fiber bridging for mixed-mode I/II delamination in CFRP multidirectional laminates. Compos Sci Technol 2017;151:302–9. http://dx.doi.org/10.1016/j.compscitech.2017.09.002.

[39] Shokrieh MM, Zeinedini A, Ghoreishi SM. On the mixed mode I/II delamination R-curve of E-glass/epoxy laminated composites. Compos Struct 2017;171:19–31. http://dx.doi.org/10.1016/j.compstruct.2017.03.017.

[40] Benzeggagh ML, Kenane M. Measurement of mixed-mode delamination fracture toughness of unidirectional glass/epoxy composites with mixed-mode bending apparatus. Compos Sci Technol 1996;56:439–49. http://dx.doi.org/10.1016/0266-3538(96)00005-X.

[41] Carreras L, Bak BLV, Turon A, Renart J, Lindgaard E. Point-wise evaluation of the growth driving direction for arbitrarily shaped delamination fronts using cohesive elements. Eur J Mech A 2018;72(October 2017):464–82. http://dx.doi.org/10.1016/j.euromechsol.2018.05.006.

[42] Bak BLV, Lindgaard E. A method for automated digital image-based tracking of delamination fronts in translucent glass fibre-laminated composite materials. Strain 2020;56(4). http://dx.doi.org/10.1111/str.12345.

[43] Tijs BH, Doldersum MH, Turon A, Waleson JE, Bisagni C. Experimental and numerical evaluation of conduction welded thermoplastic composite joints. Compos Struct 2022;281(November 2021):114964. http://dx.doi.org/10.1016/j.compstruct.2021.114964.

[44] Renart J, Leciñana I, Tijs B, Turón A, Zurbitu J. Characterization and analysis of the mode II interlaminar fatigue behaviour of thermoplastic composites considering R-curve effects. 2024, in preparation.

[45] Pérez-Galmés M, Renart J, Sarrado C, Costa J. Suitable specimen dimensions for the determination of mode II fracture toughness of bonded joints by means of the ELS test. Eng Fract Mech 2018;202(February):350–62. http://dx.doi.org/10.1016/j.engfracmech.2018.07.039.

[46] Greenhalgh ES, Hiley M, Qineti Q. Fatigue failures of polymer composites. In: Failure analysis and fractography of polymer composites. 2009, p. 238–78. http://dx.doi.org/10.1533/9781845696818.238, chap. 5.

[47] Daneshjoo Z, Shokrieh MM, Fakoor M, Alderliesten R, Zarouchas D. Physics of delamination onset in unidirectional composite laminates under mixed-mode I/II loading. Eng Fract Mech 2019;211(September 2018):82–98. http://dx.doi.org/10.1016/j.engfracmech.2019.02.013.

[48] Ferreira Motta R, Alderliesten R, Yutaka Shiino M, Odila Hilário Cioffi M, Jacobus Cornelis Voorwald H. Scrutinizing interlaminar fatigue loading cycle in composites using acoustic emission technique: Stress ratio influence on damage formation. Composites A 2020;138(May):1–11. http://dx.doi.org/10.1016/j.compositesa.2020.106065.

[49] Brunner AJ, Alderliesten R, Pascoe JA. In-service delaminations in FRP structures under operational loading conditions: Are current fracture testing and analysis on coupons sufficient for capturing the essential effects for reliable predictions? Materials 2023;16(1). http://dx.doi.org/10.3390/ma16010248.

[50] Pascoe JA, Rans CD, Benedictus R. Characterizing fatigue delamination growth behaviour using specimens with multiple delaminations: The effect of unequal delamination lengths. Eng Fract Mech 2013;109:150–60. http://dx.doi.org/10.1016/j.engfracmech.2013.05.015.

[51] Pascoe JA. Slow-growth damage tolerance for fatigue after impact in FRP composites: Why current research won't get us there. Procedia Struct Integr 2020;28:726–33. http://dx.doi.org/10.1016/j.prostr.2020.10.084.

[52] Cameselle-Molares A, Vassilopoulos AP, Keller T. Experimental investigation of two-dimensional delamination in GFRP laminates. Eng Fract Mech 2018;203(May):152–71. http://dx.doi.org/10.1016/j.engfracmech.2018.05.015.

[53] Cameselle-Molares A, Vassilopoulos AP, Renart J, Turon A, Keller T. Numerical simulation of two-dimensional in-plane crack propagation in FRP laminates. Compos Struct 2018;200(May):396–407. http://dx.doi.org/10.1016/j.compstruct.2018.05.136.